1 **NUMERICAL ASSESSMENT OF EXTERNAL SULFATE ATTACK IN**
2 **CONCRETE STRUCTURES. A REVIEW.**
3

4 Tai Ikumi[a],* and Ignacio Segura[a,b]
5

6 [a] Department of Civil and Environmental Engineering, Universitat Politècnica de
7 Catalunya Barcelona Tech, Jordi Girona 1-3, C1, E-08034 Barcelona, Spain
8

9 [b] Smart Engineering, Jordi Girona 1-3 K2M 202c, Barcelona, Spain
10

11 * Corresponding author: Tai Ikumi. Department of Civil and Environmental
12 Engineering, Universitat Politècnica de Catalunya Barcelona Tech, Jordi Girona 1-3,
13 C1, E-08034 Barcelona, Spain. Email address: tai.ikumi@upc.edu, Tel: +34 93 401
14 6507 Fax: +34 93 401 1036
15
16

17 **ABSTRACT**
18
19

20 The slow progress of the external sulfate attack and the large size and criticality of
21 typical structures affected by this phenomenon establish numerical modeling as a key
22 tool to assess the future evolution of concrete structures exposed to sulfate-rich
23 environments. The present review examines a selection of the most relevant numerical
24 models developed during the last two decades to identify and explain the principles and
25 simulation approaches commonly adopted. Assumptions associated with each approach
26 are described to fully disclose the limitations and capabilities of each model. Guidance
27 on model selection is provided based on the outcomes required. Finally, major areas
28 holding significant potential to improve the reliability of the predictions are identified
29 and discussed.
30
31

32 **Keywords**: Sulfate Attack (C), Concrete (E), Durability (C), Modeling (E)
33
34

35 **1. INTRODUCTION**
36
37

38 External sulfate attack (ESA) is a degradation process that compromises the durability
39 of concrete elements exposed to sulfate environments. There is certain controversy on
40 which mechanisms are associated with the term ESA. In this paper, ESA refers to the
41 degradation caused by the chemical reactions triggered by sulfate ingress that results in
42 the mass formation of expansive products and the dissolution of calcium-bearing
43 phases. These chemical processes might lead to cracking, progressive reduction of
44 strength and stiffness, overall expansion and mechanical failure inside or outside the

45 region directly affected by the sulfate penetration [1–3]. Even though surface scaling of
46 concrete due to crystallization of water-soluble sulfate salts is an important degradation
47 process where sulfates are involved, here are not included in the term ESA.
48
49
50 Foundations, nuclear or industrial waste containments and tunnel linings have been
51 affected by ESA. The large size and criticality of these structure elements limit the
52 efficiency of common remedial actions, often placing the monitoring of the structural
53 behavior as the only possible procedure. This scenario prompted the industry to seek
54 ways to optimize the assessment of ESA in existing properties and established the
55 development of reliable prediction models as a key challenge for structural durability.
56
57
58 Several simplified empirical and mechanistic relations were developed during the 1980s
59 and 1990s. Empirical relations refer to analytical models based on direct observations,
60 measurements or extensive experimental data records while mechanistic relations are
61 those procedures based on a simplified understanding of the attack mechanisms. Most
62 of them were derived from accelerated laboratory tests performed with small-scale
63 specimens within a framework of a limited understanding of the mechanisms associated
64 with the attack and poor computational capabilities. In general, early models were
65 developed to predict the penetration of the sulfate degradation depth [4–6] and later
66 evolved towards the estimation of the evolution of expansions [7–10].
67
68
69 The main drawback associated with empirical models is their limited applicability, as
70 these are only valid for elements subjected to the same conditions used in the tests
71 (usually small specimens in highly aggressive environments). On the other hand, most
72 simplified mechanistic models present over-simplified approaches that neglect
73 important aspects of the attack, such as the size of the structure or the interactions
74 between damaged and undamaged regions of the element. Consequently, empirical and
75 simplified mechanistic relations struggle to provide reliable predictions of the long-term
76 performance.
77
78
79 Since the early 2000s, the efforts on numerical modeling have shifted towards a more
80 comprehensive simulation of the different processes involved during the attack. Ionic
81 transport, chemical reactions and micro and macro-structural damage are computed
82 through advanced iterative calculations. The use of complex algorithms improve the
83 capacity of the models to reproduce the specific field conditions found in practice,
84 which allows more realistic predictions.
85
86
87 However, discrepancies on the general perception of ESA, computational procedures
88 and particular mechanisms of the attack (expansion mechanisms or the role of gypsum,

amongst others) led to the development of a large pool of advanced numerical models based on a wide variety of approaches. The complexity inherent to the set of principles adopted by each model and the common practice of neglecting a full disclosure of the associated assumptions and limitations often confuse practitioners and prevent them from being used.

The present paper aims to shed light on ESA modeling in order to inform practitioners of assessment tools and ultimately provide assistance for the selection of the most appropriate modeling alternative for each application. The understanding of the simplifications and hypotheses assumed by the models is not possible without a profound knowledge on the real phenomena. For that, the first section of this paper is devoted to describe all the processes involved during the attack and introduce the main uncertainties that have been later reflected in the models developed.

A selection of the most relevant numerical models developed over the last 20 years to evaluate ESA are reviewed. The scope of this review is to emphasize the capabilities and limitations of the different models based on the simulation approach adopted to reproduce the different processes involved during the attack. Guidance on ESA model selection is provided based on the capabilities of the models in terms of the outputs provided. Finally, major areas that currently compromise the accuracy of the assessments are identified and discussed. It should be emphasized that this review is strictly limited to those numerical models that incorporate iterative calculation schemes. A survey of empirical or simplified mechanistic relations is beyond the scope of this paper and can be found elsewhere [1].

2. FUNDAMENTALS OF THE EXTERNAL SULFATE ATTACK

Most research on complex degradation processes is usually focused on specific aspects of the attack, as it is often unbearable to perform a meaningful study of the overall phenomenon. This necessary approach might unintentionally lead to over simplified perceptions of ESA, which is often directly or indirectly categorized as a pure chemical or physical phenomenon.

This section aims to disclose the full extent of ESA in order to set the foundation to understand and discuss the simplifications or hypotheses assumed by the numerical models reviewed in the following sections. Even though ESA might compromise the durability of a wide variety of cement-based structures [1,2], Figure 1 illustrates a group of end bearing piles before and after the attack to depict a schematic representation of the different mechanisms involved, specifying the scale at which these are developed.

133　The attack can be divided in four main processes: transport, chemical reactions,
134　expansive forces and the mechanical response.
135
136
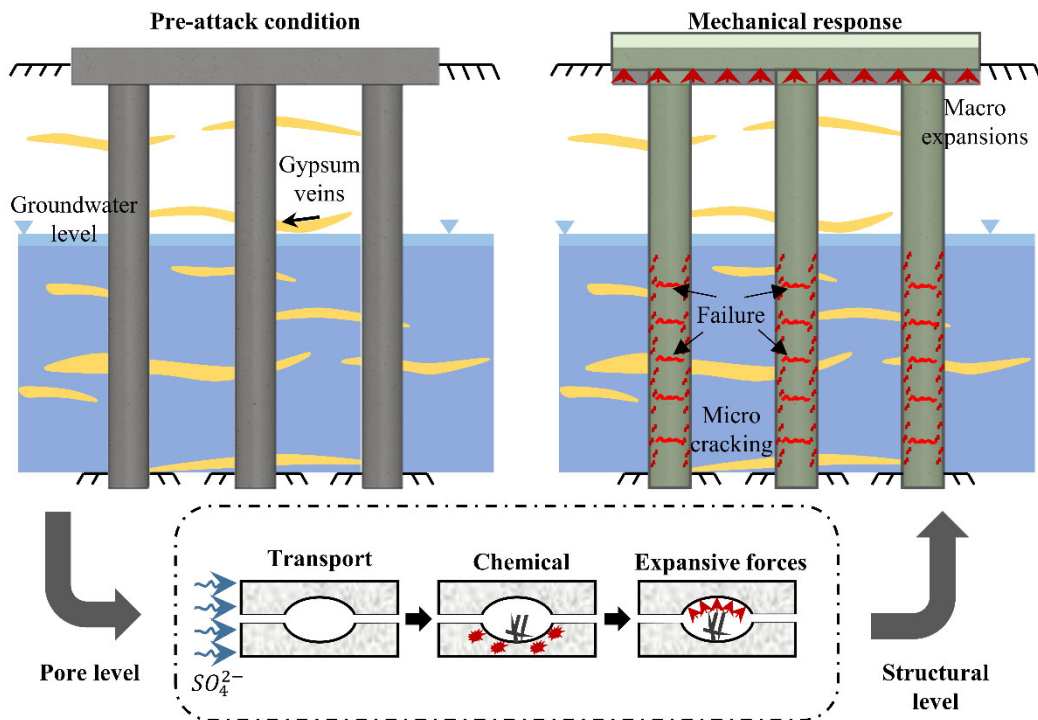
137
138
139
140　**2.1. Transport process**
141
142
143　The development of ESA requires the penetration of sulfate ions from an external
144　source into the cement paste fraction of the concrete. For that, the open porosity of the
145　concrete structure has to be in direct contact with a sulfate-rich media. The connection
146　between the external aqueous media and the pore solution alter the equilibrium
147　conditions in the liquid system, leading to a net mass flow. The characteristics of the
148　mass flow can be described based on the saturation level of the pore structure.
149
150
151　In saturated conditions and under no pressure gradients, sulfate penetration and other
152　ionic fluxes are mainly driven by electrochemical potential gradients (chemical and
153　electrical potential) [11]. The chemical potential difference, usually referred to as
154　diffusion, transfers charged solutes from areas of high concentration to areas of lower
155　concentration. Electrical potential gradients are generated in the pore solution due to the
156　different speeds of the charged solutes. Faster ions create an electric field that slows
157　these ions down and accelerates the slower ones to preserve the electroneutrality
158　throughout the liquid system [11].
159

160

161 Besides the electrochemical potential gradients, there are other transport mechanisms
162 that might also affect the movement of ionic species in saturated conditions. In non-
163 isothermal systems, temperature gradients promote ionic flux by a phenomenon usually
164 referred to as Soret effect or thermal diffusion [12]. Finally, the flux of ionic species
165 might be altered by chemical activity effects related to ion/ion and ion/solvent
166 interactions when the ionic strength of the pore solution is high [13].

167

168

169 In unsaturated conditions, ionic transport also occurs indirectly by liquid movement
170 from the external media into the pore network. The sulfate-rich aqueous solution is
171 absorbed into the interior of the material by capillary forces arising from the contact of
172 the pores of the material with the liquid phase [11,14]. Notice that under full saturation
173 conditions this phenomenon should not be considered as the velocity of the liquid is
174 null. However, in partially saturated concrete subjected to drying-wetting cycles at the
175 surface, the sulfate ingress caused by moisture flux should not be disregarded.

176

177

178 **2.2. Chemical reactions**

179

180

181 The reactive system of cementitious materials is composed of the aqueous pore solution,
182 vapor phase inside the pores and the unhydrated and hydrated solid phases of the
183 cement paste (aggregates are usually considered inert). According to the second law of
184 thermodynamics, in isolated conditions the different components tend to be in
185 equilibrium to minimize the internal energy of the system. However, the mass fluxes
186 caused by the interaction between the external aqueous media and the reactive system
187 during ESA modify the position of the equilibrium state and promote a series of
188 chemical reactions to restore minimum energy in the system.

189

190

191 The chemical reactions triggered during ESA vary depending on the sulfate salt present
192 in the external media. The influence of the sulfate salt on the chemical reactions and
193 subsequent damage generated can be explained in terms of solubility and interaction
194 between the cation of the salt and the other reactive compounds of the system. The main
195 salts associated with ESA are sodium sulfate (Na_2SO_4), calcium sulfate ($CaSO_4$) and
196 magnesium sulfate ($MgSO_4$) [15]. Table 1 shows the solubility of the salts in water at
197 20 ºC and the maximum sulfate concentration potentially reached in solutions saturated
198 with each salt. The solubility of $CaSO_4$ is about 100 times smaller than the solubility of
199 Na_2SO_4 or $MgSO_4$. The high stability of this salt reduces the maximum sulfate
200 concentration in solution to about 1.5 g/l, which greatly limits the deleterious effects
201 caused by this form of attack. On the other hand, the damage generated by Na_2SO_4 and
202 $MgSO_4$ solutions might be more significant due to the potential high sulfate
203 concentrations and crystallization pressures developed during the attack.

204

205

206   Table 1. Solubility in water at 20ºC and sulfate concentration in saturated conditions

207   [16].

Sulfate salt	Solubility (g/l)	$[SO_4^{2-}]_{aq}$ (g/l)
Na_2SO_4	195.0	131.9
$CaSO_4 \cdot 2H_2O$	2.6	1.5
$MgSO_4$	337.0	268.9

208

209

210   ESA caused by magnesium sulfate is strongly influenced by the presence of magnesium
211   ions in solution from the sulfate salt. The formation of magnesium hydroxide lowers the
212   pH of the pore solution, which promotes the transformation of the C-S-H gel into a M-
213   S-H phase without binding properties. This transformation causes softening and
214   disintegration of the matrix and the formation of gypsum and brucite. A review of the
215   chemical reactions related to magnesium sulfate environments can be found in [17].

216

217

218   ESA caused by sodium sulfate follows a completely different damage mechanism,
219   characterized by ettringite and gypsum formation in such a quantity that the material
220   sustains physical and chemical damage. Physical damage is usually related to the
221   generation of expansive forces at the pore-level, which are explained in detail in section
222   2.3. Chemical damage refers to the degradation of mechanical properties in the
223   cementitious matrix of the hardened concrete caused by the chemical reactions triggered
224   by sulfate penetration.

225

226

227   The most commonly reported reactions are listed in Table 2 [9,18,19]. Eqs. (1) - (3)
228   describe the reactions between sodium sulfate ions with portlandite (CH), tricalcium
229   aluminate (C$_3$A) and monosulfate (C$_4$A$\overline{S}$H$_{12}$) to form gypsum (C$\overline{S}$H$_2$), ettringite
230   (C$_6$A$\overline{S}_3$H$_{32}$) and sodium hydroxide (NaOH). Gypsum is only formed in certain sulfate
231   concentrations and pH conditions of the solution. High sulfate concentrations lead to the
232   precipitation of gypsum, while lower sulfate concentrations lead to no or very little
233   gypsum precipitation [20,21]. The gypsum precipitated in Eq. (1) may react with the
234   hydrated aluminate phases, namely tricalcium aluminate, tetracalcium aluminate hydrate
235   (C$_4$AH$_{13}$), monosulfate and hydrogarnet (C$_3$AH$_6$) to produce ettringite, as summarized
236   in Eqs. (4) - (7).

237

238

239   Even though some researchers suggest that sodium ions in solution could modify the
240   solubility of the silicate phases and alter the morphology of the C-S-H gel [22,23], it is
241   generally accepted that the presence of sodium from the sulfate salt does not

242 significantly alter the development of the attack. As described in Eqs. (1) - (7), gypsum
243 and ettringite formation requires calcium which is mainly obtained by the dissolution of
244 calcium hydroxide. However, at late stages of the attack or under shortage of
245 portlandite, calcium might be obtained from C-S-H gel. The C-S-H phase is responsible
246 for strength and stiffness in the cementitious matrix and its dissolution might cause a
247 mechanical strength loss and micro-crack formation.
248
249
250 Table 2. Main chemical reactions related to ESA caused by Na_2SO_4 salts and

251 corresponding expansion factors.

Primary reactive	Chemical reaction	Eq.	Expansion factor
CH	$CH + Na_2SO_4 + 2H \rightarrow C\bar{S}H_2 + 2NaOH$	(1)	1.27
C_3A	$C_3A + 3Na_2SO_4 + 3CH + 32H \rightarrow 6NaOH + C_6A\bar{S}_3H_{32}$	(2)	2.76
$C_4A\bar{S}H_{12}$	$3C_4A\bar{S}H_{12} + 3Na_2SO_4 \rightarrow 6NaOH + 2Al(OH)_3 + 21H + 2C_6A\bar{S}_3H_{32}$	(3)	0.52
C_3A	$C_3A + 3C\bar{S}H_2 + 26H \rightarrow C_6A\bar{S}_3H_{32}$	(4)	1.25
C_4AH_{13}	$C_4AH_{13} + 3C\bar{S}H_2 + 14H \rightarrow C_6A\bar{S}_3H_{32} + CH$	(5)	0.48
$C_4A\bar{S}H_{12}$	$C_4A\bar{S}H_{12} + 2C\bar{S}H_2 + 16H \rightarrow C_6A\bar{S}_3H_{32}$	(6)	0.54
C_3AH_6	$C_3AH_6 + 3C\bar{S}H_2 + 2OH \rightarrow C_6A\bar{S}_3H_{32}$	(7)	0.89

252
253
254
255 **2.3. Expansive forces**
256
257
258 It is well established that certain chemical reactions between the pore solution and the
259 cement paste generate expansive forces at the pore-level. These are primarily
260 responsible for the "visible" consequences of the ESA, such as expansion, cracking and
261 spalling of the hardened material [1]. However, there is still no agreement on the
262 expansion mechanism underlying the degradation typically observed. Several
263 mechanisms have been suggested in the literature to explain how some
264 precipitation/dissolution processes are converted into actual expansions. A
265 comprehensive review of the suggested theories can be found in [1,24]. Here, the two
266 theories that stand as the most discussed are described in detail.
267
268
269 *2.3.1. Volume increase approach*
270
271
272 The volume increase approach assumes that the expansions observed are the result of
273 the additional volume generated by the expansive products precipitated during the
274 attack [9,18]. Expansive products are defined as those phases that take up more space

275 than the volume used by the reactants consumed for its formation. Usually, the
276 numerical expression described in Eq. (8) is adopted to quantify an expansion factor (v)
277 [9].
278
279

$$v = \frac{\sum solid\ product\ volumes - \sum solid\ reactant\ volumes}{\sum solid\ reactant\ volumes} \tag{8}$$

280
281
282 As indicated by Eq. (8), only the volume occupied by solid reactants and products are
283 considered. This assumes that the aqueous species consumed during the reaction (e.g.
284 water molecules) are instantly replaced by new molecules entering the system from an
285 external source. Table 2 includes the expansion factors (v) of the main chemical
286 reactions involved during the ESA. The molar volumes of all phases considered in the
287 calculations are shown in Table 3. The molar volumes of Na_2SO_4, NaOH and $Al(OH)_3$
288 are not considered as it is assumed that these species are dissolved in the aqueous phase.
289
290
291 Table 3. Molar volumes of the mineral phases.

Mineral phase	Name	Molar volume (V_m) [cm³/mol]
$C_6A\bar{S}_3H_{32}$	Ettringite	707 [25]
C_3AH_6	Hydrogarnet	150 [25]
$C_4A\bar{S}H_{12}$	Monosulfate	309 [25]
C_4AH_{13}	Tetracalcium aluminate hydrate	274 [25]
CH	Portlandite	33 [26,27]
$C\bar{S}H_2$	Gypsum	75 [26,27]
C_3A	Tricalcium aluminate	89 [25]

292
293
294 Linear expansion associated with each expansive chemical reaction listed in Table 2 can
295 be estimated by multiplying the corresponding expansion factor (v), the molar volume
296 (V_m) and the molar concentration of solid reactants consumed (CA^r) [18]. Total linear
297 expansions (ε_l) triggered during ESA are defined as the sum of expansions associated to
298 each chemical reaction considered (Eq. (9)). In Eq. (9), the term n corresponds to the
299 number of chemical reactions considered.
300
301

$$\varepsilon_l = \sum_{i=1}^{n} \left[\left(1 + v_i V_{m,i} CA_i^r \right)^{1/3} - 1 \right] \tag{9}$$

302
303
304 At present, there is no experimental evidence suggesting that expansions can be entirely
305 explained by the additional volume generated from ettringite or gypsum formation.
306 Even though Kunther et al. stated that there seems to be a link between the coexistence

307   of ettringite and gypsum and the tendency for expansion [24], a direct connection
308   between the amount of expansive phases formed and expansion generated has not been
309   documented.

310

311

312   *2.3.2. Crystallization pressure theory*

313

314

315   The crystallization pressure theory states that expansions are caused by the
316   crystallization pressure exerted on the pore walls due to the formation of ettringite
317   [28,29]. In this case, the driving force promoting the degradation during the ESA are the
318   high activities of the reactants. The pressure (p) exerted by an ettringite crystal of molar
319   volume (V_{Et}) may be expressed by Eq. (10) [30]. The term R corresponds to the gas
320   constant, T is the absolute temperature and K_{Et} is the equilibrium constant of ettringite.
321   The ionic activity product of ettringite (Q_{Et}) might be calculated as indicated in Eq.
322   (11).

323

324

$$p = \frac{RT}{V_{Et}} \ln\left(\frac{Q_{Et}}{K_{Et}}\right) \tag{10}$$

$$Q_{Et} = (C_{Ca^{2+}}\gamma_{Ca^{2+}})^6 \left(C_{Al(OH)_4^-}\gamma_{Al(OH)_4^-}\right)^2 (C_{OH^-}\gamma_{OH^-})^4 \left(C_{SO_4^{2-}}\gamma_{SO_4^{2-}}\right)^3 \left(C_{H_2O}\gamma_{H_2O}\right)^{26} \tag{11}$$

325

326

327   There are two necessary conditions for expansion to occur [28,30]. First, the ettringite
328   crystal must be growing from a supersaturated solution ($Q_{Et} > K_{Et}$). Otherwise, the
329   pressure obtained by Eq. (10) equals 0 or negative. Second, the crystal must grow in
330   confined conditions and exert the expansive forces to the pore walls in order to convert
331   the chemical energy into mechanical work. This condition explains why not all
332   ettringite formed is expansive, as the crystals need to be confined in order to exert
333   pressure.

334

335

336   The pressure at the crystal/liquid interface (p) can be also expressed in terms of the
337   interfacial free energy (γ_{CL}) for a particular crystal curvature (κ_{CL}). Eq. (12) states that
338   at equilibrium, the energetic condition of the atoms on the surface of a crystal due to its
339   morphology is balanced with the concentration of ions in the adjacent solution. Several
340   researchers have used this relation to assess the influence of crystal size and shape on
341   the potential crystallization pressure developed during ettringite growth in confined
342   conditions [29–32].

343

344

$$p = \kappa_{CL}\gamma_{CL} = \frac{RT}{V_{crystal}} \ln\left(\frac{Q_{Et}}{K_{Et}}\right) \tag{12}$$

347 Eq. (12) indicates that small crystals with high curvatures are in equilibrium with a
348 higher concentration than larger macroscopic crystals. Consequently, small crystals
349 potentially generate higher crystallization pressures as long as sulfate supply is not
350 restricted. On the other hand, large crystals are unable to exert significant pressures and
351 therefore, are unlikely to be the origin of damage [31,32]. Accordingly, the expansive
352 force developed during sulfate attack is mainly determined by the locations of ettringite
353 growth in the microstructure rather than the total volume of ettringite formed [29,33].

356 The crystallization pressure theory has been thoroughly discussed from a theoretical
357 standpoint in several publications (e.g. [28,29,34]). However, experimental evidences
358 that support this theory for the specific case of the ESA are still scatter. Notice that to
359 estimate crystallization pressures by Eq. (10), one needs to measure the composition of
360 the pore solution at different locations within the pore network of the specimen, which
361 is currently not possible [34]. Several authors have attempted to quantify crystallization
362 pressures generated during ESA by alternative experimental approaches [32,34].
363 Despite the promising results, no author has been able to validate those pressures by
364 reproducing the macroscopic expansions measured experimentally.

367 **2.4. Mechanical response**

370 Sections 2.2 – 2.3 described a series of processes occurring at the pore-level during
371 ESA that leads to chemical degradation and the generation of expansive forces in the
372 hardened matrix of the material. However, the description of these phenomena does not
373 quantify the actual mechanical consequences associated, as chemical reactions per se
374 are not necessarily harmful [35]. To account for that, the dissolution of calcium-bearing
375 phases and the expansive forces generated should be translated into some sort of
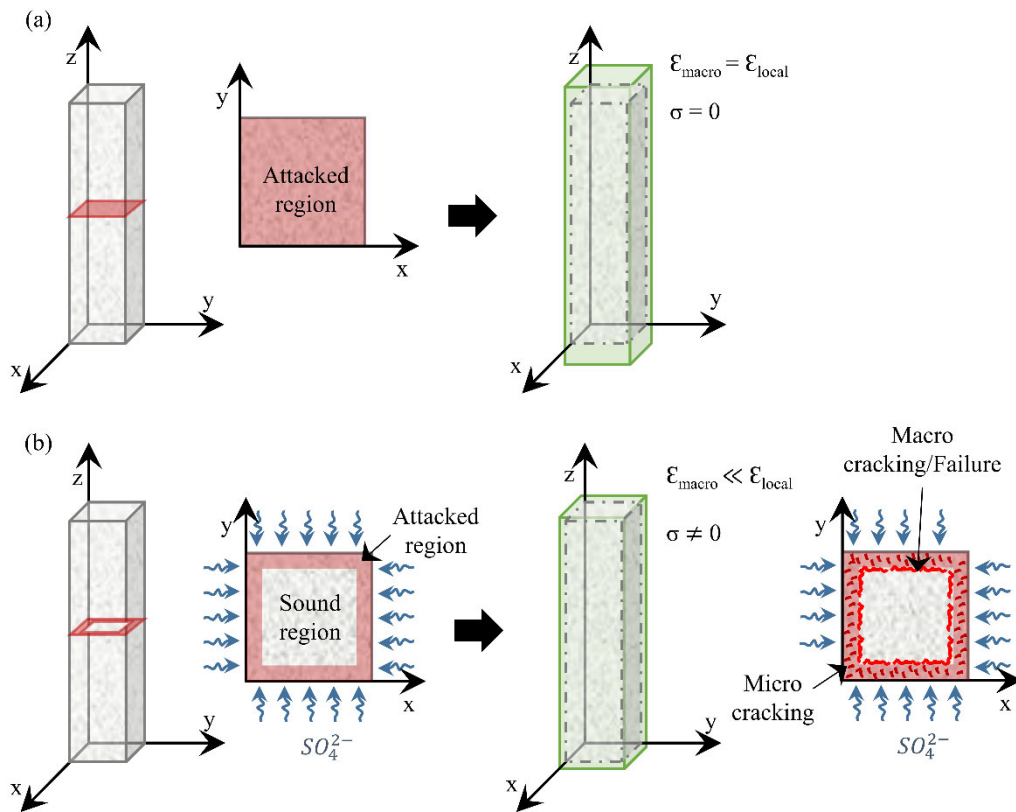376 physical and chemical damage and macroscopic expansions.

379 If ESA was an internal attack that affected uniformly all the element or structure, the
380 local mechanical response of the material would be representative of the macroscopic
381 behavior of the element. This scenario is depicted in Figure 2a, where ε_{macro} and ε_{local}
382 correspond to macroscopic and local expansions, respectively.

(a)

z

y

Attacked region

x

z $\varepsilon_{macro} = \varepsilon_{local}$

$\sigma = 0$

y

x

(b)

z

y Attacked region

Sound region

x

SO_4^{2-}

z $\varepsilon_{macro} \ll \varepsilon_{local}$

$\sigma \neq 0$

y

x

Macro cracking/Failure

y

Micro cracking

x

SO_4^{2-}

385
386
387
388   However, the degradation caused by ESA progresses gradually from the external
389 surface towards the inner layers of the material, as sulfate ions penetrate and react with
390 compounds from the hydrated cement paste. Consequently, a multi-layered pattern is
391 formed with an external damaged layer and an internal sound core (Figure 2b). In this
392 case, the expansive forces generated at the pore level within the attacked region cannot
393 be fully released by deformations since the sound core of the element acts as a
394 restriction to maintain compatibility. Because of that, the macroscopic expansions
395 developed are usually considerably lower than the local expansions generated. In fact,
396 due to the large sound/attacked region ratios commonly observed in field conditions,
397 significant macro expansions are rarely reported. Moreover, the mechanical interaction
398 between sound and damage regions generates an auto-balanced tension state, leading to
399 microcracking in the attacked region due to compressive stresses and possible
400 mechanical failures outside the zone directly affected by the sulfate penetration.

401
402

403 **3. COMPUTER-BASED MODELS FOR ESA ASSESSMENT**

404
405

406   This section reviews a selection of the most relevant numerical models developed
407 during the last 20 years that incorporate complex iterative calculation schemes to assess
408 the deleterious effects of ESA. This review does not aim to describe in detail each one
409 of the assessment methods. Instead, the capabilities and limitations of the different

410 options are examined based on how the different processes involved during the attack
411 are simulated. Table 4 lists all models evaluated in this review and classifies them based
412 on the processes considered: transport (T), chemical reactions (C), expansive forces (E)
413 and mechanical response (M). Pure transport or chemical models are not included in
414 this review.

415
416

417 Table 4 highlights that not all advanced ESA models simulate aspects related to the
418 main processes involved during the attack (T,C,E,M). Early models focused efforts on
419 the modeling of the reactive-transport phenomenon (identified as T-C in Table 4).
420 Evaluations based on this approach indirectly perceives ESA solely as a chemical attack
421 and assumes that the deleterious effects can be assessed by the study of the transport
422 process and the chemical reactions triggered, without converting the chemical reactions
423 into actual damage or strength loss.

424
425
426   Table 4. ESA processes simulated by the assessment tools.

Authors	Year	Ref.	Transport (T)	Chemical reactions (C)	Expansive forces (E)	Mechanical response (M)	Category
P.N. Gospondinov et al.	1999	[36]	X	X			T-C
F. Schmidt-Döhl & F.S. Rostasy	1999	[37,38]	X	X	X	X	T-C-E-M
M.K. Mironova et al.	2002	[39]	X	X			T-C
R. Tixier & B. Mobasher	2003	[18,40]	X	X	X	X	T-C-E-M
Y. Maltais et al.	2004	[21]	X	X			T-C
E. Rigo et al.	2005	[41]	X	X	X	X	T-C-E-M
M.A. Shazali et al.	2006	[42]	X	X		X	T-C-M
E. Samson & J. Marchand	2007	[43]	X	X			T-C
B. Bary	2008	[44]	X	X	X	X	T-C-E-M
M. Basista & W. Weglewski	2009	[45]	X	X	X	X	T-C-E-M
B. Lothenbach et al.	2010	[20]	X	X			T-C
S. Sarkar et al.	2010	[19]	X	X	X	X	T-C-E-M
A. Idiart et al.	2011	[46]	X	X	X	X	T-C-E-M
X.-B. Zuo et al.	2012	[47]	X	X	X		T-C-E
B. Bary et al.	2014	[48]	X	X	X	X	T-C-E-M
T. Ikumi et al.	2014	[49]	X	X	X	X	T-C-E-M
Y. Yu et al.	2015	[50]	X	X	X	X	T-C-E-M
N. Cefis & C. Comi	2017	[51]	X	X	X	X	T-C-E-M
J. Zhang et al.	2017	[52]	X	X	X	X	T-C-E-M

427
428

429 T-C-E models incorporate the simulation of the expansive forces generated at the pore-
430 level. By that, it is acknowledged both the chemical and physical nature of ESA.
431 However, similarly to T-C models, the chemical reactions or the expansive forces
432 monitored are not converted into actual damage and strains. During the last decade, a
433 significant number of models have introduced mechanical aspects to quantify the
434 damage generated and/or the macro-scale response of the attacked element. Models that
435 only account for the chemical damage are identified as T-C-M in Table 4. Models that

436   quantify the degradation caused by both the chemical reactions and the expansive forces
437   generated at the pore-level are identified as T-C-E-M.
438
439
440   The following sections present an in-depth analysis of the modelization approaches
441   adopted by these models to simulate the transport process, chemical reactions,
442   expansive forces and the mechanical response associated to the ESA.
443
444
445   **3.1. Modeling of the transport process**
446
447
448   As introduced in section 2.1, ionic transport between the liquid phase in the external
449   media and the pore solution might be caused by two main processes: electrochemical
450   potential gradients and advection. The unidirectional flux of each ionic species present
451   in solution (F_i) can be expressed as in Eq. (13), where the first term refers to the
452   electrochemical effects and the second term quantifies the ionic transport due to
453   aqueous solution motion.
454
455

$$F_i = -\frac{D_i^0}{RT} c_i \frac{\partial}{\partial x}(\mu_i) + c_i v \tag{13}$$

456
457
458   In Eq. (13), c_i, D_i^0 and μ_i refers to the concentration, the diffusion coefficient and the
459   electrochemical potential of the ionic species i, respectively. R is the ideal gas constant,
460   T is the thermodynamic temperature and v is the velocity of the liquid phase. The
461   electrochemical potential μ_i is defined as indicated in Eq. (14).
462
463

$$\mu_i = \mu_i^0 + RT\ln(\gamma_i c_i) + z_i F\psi \tag{14}$$

464
465
466   The terms μ_i^0, γ_i and z_i correspond to the electrochemical potential in the standard state,
467   the chemical activity coefficient and the valence number of the ionic species i,
468   respectively. F is the Faraday constant and ψ is the electrical potential. Substituting Eq.
469   (14) into Eq. (13) yields the general ionic transport equation (Eq. 15) [43].
470
471

$$F_i = -D_i^0 \frac{\partial c_i}{\partial x} - \frac{D_i^0 z_i F}{RT} c_i \frac{\partial \psi}{\partial x} - D_i^0 c_i \frac{\partial \ln \gamma_i}{\partial x} - \frac{D_i^0 c_i \ln(\gamma_i c_i)}{T} \frac{\partial T}{\partial x} + c_i v \tag{15}$$

472
473

474 The mass conservation equation must be introduced into Eq. (15) to obtain the time-
475 dependent response of the system. The unidirectional mass equation for an ionic species
476 diffusing through an infinitesimal layer of liquid phase with thickness ∂x can be
477 expressed as indicated in Eq. (16). The combination of Eq. (15) and Eq. (16) gives the
478 complete mass transport equation (Eq. (17) [43]). Reactions taking place solely in the
479 liquid phase (homogenous reactions) are usually neglected in ESA models and are not
480 considered in this formulation.

481

482

$$\frac{\partial c_i}{\partial t} = -\frac{\partial F_i}{\partial x} \tag{16}$$

$$\frac{\partial c_i}{\partial t} = \frac{\partial}{\partial x}\left(D_i^0 \frac{\partial c_i}{\partial x} + \frac{D_i^0 z_i F}{RT} c_i \frac{\partial \psi}{\partial x} + D_i^0 c_i \frac{\partial \ln\gamma_i}{\partial x} + \frac{D_i^0 c_i \ln(\gamma_i c_i)}{T}\frac{\partial T}{\partial x} - c_i v\right) \tag{17}$$

483

484

485 Notice that Eq. (17) refers to the transport of ions in the liquid phase. However, solving
486 the equations at the pore scale requires the consideration of the exact geometry of the
487 pore network, which is currently impossible. Instead, Eq. (17) is usually solved at the
488 structure level. For that, the different components within a volumetric unit of concrete
489 are considered. Concrete is composed by a solid matrix and a pore network, which can
490 be fully or partially saturated with aqueous phase. In the case of being partially
491 saturated, vapor should be also accounted as a component of concrete. Samson and
492 Marchand applied an averaging technique to cementitious materials and proposed Eq.
493 (18) as the averaged form of Eq. (17) [43].

494

495

$$\frac{\partial(wC_i)}{\partial t} = \frac{\partial}{\partial x}\left(\underbrace{D_i w \frac{\partial C_i}{\partial x}}_{i} + \underbrace{\frac{D_i z_i F}{RT} wC_i \frac{\partial \psi}{\partial x}}_{ii} + \underbrace{D_i wC_i \frac{\partial \ln\gamma_i}{\partial x}}_{iii} + \underbrace{\frac{D_i C_i \ln(\gamma_i C_i)}{T} w\frac{\partial T}{\partial x}}_{iv} - \underbrace{C_i V}_{v}\right) - R \tag{18}$$

496

497

498 The uppercase parameters C_i and V correspond to the average of the corresponding
499 quantity in Eq. (17). D_i is the diffusion coefficient at the macroscopic level, which
500 differs from D_i^0 by the consideration of the geometrical complexity of the pore network.
501 The averaging process introduces the additional term w to account for the volumetric
502 water content. In saturated conditions this term can be assumed to be equal to the
503 connected porosity of the material. However, the consideration of this term in non-
504 saturated conditions requires the modeling of moisture levels or the liquid water
505 content. Details on the different approaches used to model moisture transport can be
506 found in [15]. The term R is introduced to account for the increase or decrease of local
507 availability of ionic species due to chemical reactions (usually dissolution/precipitation
508 processes). The different approaches to model the chemical reactions (R) are explained
509 in section 3.2.

512 Eq. (18) provides a comprehensive mathematical framework to simulate the ionic
513 transport associated to ESA based on the interaction of five transport mechanisms:
514 diffusion (i), electrical potential (ii), chemical activity (iii), temperature and (iv)
515 advection (v). However, ESA models rarely consider all mechanisms listed. Table 5
516 examines the main characteristics of the transport modules included in the numerical
517 models evaluated, grouped by the categories defined in Table 4. While the diffusion
518 mechanism is simulated in all models reviewed, advection, electrical coupling and
519 chemical activity are only considered in about 50, 25 and 20 % of the models,
520 respectively.

521
522
523 Table 5. Characteristics of the transport models included in ESA models.

	Ref.	Mechanisms				Saturation level		Ionic species		Diffusion coef.	
		Diffusion	Electrical coupling	Chemical activity	Advection	Saturated	Non-saturated	Single-ionic	Multi-ionic	Damage	Porosity change
T-C	[36]	X				X		X			X
	[39]	X			X	X		X			X
	[21]	X	X	X	X		X		X		X
	[43]	X	X	X	X		X		X		X
	[20]	X				X			X		X
T-C-E	[47]	X				X		X			X
T-C-M	[42]	X			X		X	X		X	X
T-C-E-M	[37,38]	X	X		X		X		X	X	X
	[18,40]	X				X		X		X	
	[41]	X	X		X		X		X	X	X
	[44]	X				X			X		X
	[45]	X				X		X		X	
	[19]	X		X		X			X	X	X
	[46]	X				X		X		X	X
	[48]	X				X			X		X
	[49]	X				X		X		X	X
	[50]	X	X	X	X		X		X	X	X
	[51]	X			X		X	X			
	[52]	X			X		X	X		X	X

524
525
526 Advection is associated to ionic transport caused by changes on moisture conditions in
527 the pores. Therefore, models that include an advection term are able to account for non-
528 saturated conditions. The only exception is the model presented by Mironova et al. [39],
529 which considers advection in fully saturated conditions. In this case, the advection is
530 attributed to the movement of ions caused by liquid push out of the capillary as a result
531 of capillary filling with solid chemical products.
532
533

534   The fewer number of models considering the effects of electrical coupling and chemical
535   activity is mainly explained by the complexity associated to the simulation of these
536   phenomena, which require a full description of the ionic species in the solution. This is
537   reflected on Table 5, where all models that simulate electrical coupling or chemical
538   activity include multi-ionic transport modules. Reported results suggest that this
539   increase of computational complexity might be justified in the case of the electrical
540   coupling, as simulations made without electrical coupling showed significant
541   discrepancies with the measurements [43,50]. However, currently there are no clear
542   evidences that justify the consideration of the chemical activity gradients in ESA
543   transport models. Yu et al. [50] obtained very similar results with and without coupling
544   the chemical activity term, which might suggest that the contributions of chemical
545   activities are not critical.

546

547

548   The main distinctive feature between reactive-transport models (T-C) and those
549   including mechanical considerations (T-C-M and T-C-E-M) is found on the formulation
550   adopted to consider the diffusion coefficient(s). All T-C models listed in Table 5 alter
551   the diffusion coefficient during the simulation based only on changes of porosity due to
552   precipitation or dissolution of solid phases. Pore filling caused by precipitation
553   processes are reflected by a reduction of diffusivity whereas increase of porosity caused
554   by dissolution processes is considered through an increase of diffusivity. A review on
555   the different approaches used to quantify the variations of diffusivity caused by porosity
556   changes can be found in [53].

557

558

559   On the other hand, most T-C-M and T-C-E-M models incorporate the effects associated
560   to damage generation on the diffusion coefficient of the ionic species. Strength loss,
561   cracking and spalling are usually reflected as an increase of diffusivity since it is
562   considered that these might introduce easier penetration paths towards the inner layers
563   of the material. These models quantify the diffusivity increase by simple relations based
564   on the bulk damage [19,38,40–42,45,49,52] or the crack width [46] generated.
565   Additionally, the model presented by Yu et al. [50] simulates the mechanism of ionic
566   diffusion in cracked cementitious materials by a combination of a traditional approach
567   (modification of diffusivity based on continuum damage mechanics) and the
568   introduction of an additional term in Eq. (18) to describe the capillary suction effect
569   brought by newly formed unsaturated cracks.

570

571

572   **3.2. Modeling of chemical reactions**

573

574

575   Table 6 summarizes the approaches used by recent advanced numerical models to
576   simulate the chemical reactions associated to the ESA, which can be based on chemical
577   kinetic laws (K), chemical equilibrium algorithms (E) or a combination of both.

Table 6. Characteristics of the chemical modules included in advanced ESA models.

| | Ref. | Species monitored | | Chemical kinetics (K) | | | Chemical equilibrium (E) | |
		Ions in solution	Solid phases	1st order	2nd order	Multi-order	Law of mass action (LMA)	Gibbs free energy min. (GEM)
T-C	[36]	Sulfate		X				
	[39]	Sulfate		X				
	[21]	Full composition	Full composition				X	
	[43]	Full composition	Full composition				X	
	[20]	Full composition	Full composition				X	
T-C-E	[47]	Sulfate	Aluminates	X				
T-C-M	[42]	Sulfate	Gypsum			X		
T-C-E-M	[37,38]	Full composition	Full composition	X				X
	[18,40]	Sulfate	Aluminates		X			
	[41]	Full composition	Full composition	X				X
	[44]	Sulfate,Calcium	Ettringite,Gypsum	X				
	[45]	Sulfate	Ettringite		X			
	[19]	Full composition	Full composition				X	
	[46]	Sulfate	Aluminates		X			
	[48]	Full composition	Full composition	X			X	
	[49]	Sulfate	Aluminates		X			
	[50]	Full composition	Full composition				X	
	[51]	Sulfate	Aluminates		X			
	[52]	Sulfate	Aluminates		X			

3.2.1. Kinetic laws

Models based on chemical kinetic laws (K) use partial differential equations with empirical reaction rate constants to estimate the precipitation of products and the consumption of reactants. Even though Table 2 describes up to seven chemical reactions typically involved during ESA, none of the models reviewed adopt this number of kinetic laws. Instead, the chemical processes are usually simplified into one or two chemical reactions to account for gypsum ($C\bar{S}H_2$) formation from portlandite (CH) and sulfate ions (SO_4^{2-}) (Eq. (19)) and/or ettringite ($C_6A\bar{S}_3H_{32}$) formation from the interaction of sulfates with the aluminate phases (Al) (Eq. (20)).

$$[CH] + [SO_4^{2-}] \rightarrow [C\bar{S}H_2] \tag{19}$$

$$a[Al] + b[SO_4^{2-}] \rightarrow c[C_6A\bar{S}_3H_{32}] \tag{20}$$
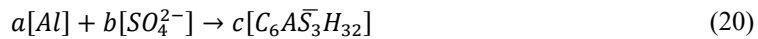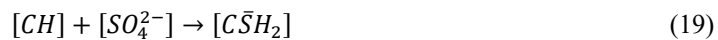
599 The aluminate phases considered vary in each model, usually being monosulfate,
600 tetracalcium aluminate hydrate, tricalcium aluminate or an equivalent grouping of the
601 previously mentioned phases. The terms *a*, *b* and *c* included in Eq. (20) correspond to
602 the specific stoichiometric coefficients of the aluminate phase, sulfates and ettringite,
603 respectively. As defined by the chemical reaction described in Eq. (1), all stoichiometric
604 coefficients in Eq. (19) are set to one.

605

606

607 According to Table 6, the majority of models based on rate laws only consider sulfate
608 and aluminate consumption [40,46,47,49,51,52] or sulfate consumption and ettringite
609 formation [45]. Both approaches are equivalent as the processes simulated correspond to
610 the same chemical reaction (Eq. (20)). On the other hand, only two models simulate
611 gypsum formation through kinetic laws [42,44]. In the early models from Gospodinov
612 et al.[36] and Mironova et al. [39], it is not clear which chemical phenomenon is being
613 modelled since only sulfate consumption is accounted. Solid phase formation is
614 indirectly quantified by the term "chemically reacted ions", without specifying to which
615 phase it refers.

616

617

618 The law of mass action states that the rate of a chemical reaction at a constant
619 temperature is directly proportional to the product of the concentrations or activities of
620 the substances that influence the rate. The sum of the exponents at which each
621 concentration term is raised defines the order of the kinetic law. Therefore, models
622 based on first-order reactions describe a rate proportional to the concentration of a
623 single reactant whereas in second-order kinetic laws the rate is proportional to the
624 concentration of two reactants. Table 6 indicates that the majority of ESA models based
625 on kinetic laws adopt either first or second-order equations, being the latter the most
626 common approach.

627

628

629 The rate law for the chemical reaction described in Eq. (19) is usually described in
630 terms of either the consumption of sulfate (Eq. (21)) or a combination of sulfate and
631 portlandite (Eq. (22)).

632

633

$$\text{rate} = \frac{\partial SO_4^{2-}}{\partial t} = -k_1[SO_4^{2-}] \tag{21}$$

$$\text{rate} = \frac{\partial SO_4^{2-}}{\partial t} = -k_2[SO_4^{2-}][CH] \tag{22}$$

634

635

636 The terms k_1 and k_2 correspond to rate constants for first and second-order reactions,
637 respectively. Different terminologies for the rate constants are used to emphasize that
638 despite both parameters belong to the same chemical reaction, its values may not be

639 equal. This is reflected on the units traditionally used, *time^{-1}* and *concentration^{-1}·time^{-1}*
640 for k_1 and k_2, respectively. Multiplying the units of k by the concentration factors
641 (expressed as square brackets) give the rate in units of *concentration·time^{-1}*. A negative
642 sign is placed before the rate as the concentration of a reactant decreases during the
643 reaction.
644
645
646 The kinetic laws used for the simulation of the chemical reaction that controls ettringite
647 precipitation (Eq. (20)) are usually defined in terms of either the sulfate concentration
648 (Eq. (23)) or the sulfate and aluminate concentration (Eq. (24)).
649
650

$$\text{rate} = \frac{\partial SO_4^{2-}}{\partial t} = -k_1 b[SO_4^{2-}] \tag{23}$$

$$\text{rate} = \frac{\partial SO_4^{2-}}{\partial t} = -k_2 b[SO_4^{2-}][Al] \tag{24}$$

651
652
653 In this case, the rate law for each reactant and product is modified by the stoichiometric
654 coefficients *a*, *b* and *c* according to the expression described in Eq. (25). Final
655 formulations of first and second-order kinetic laws for aluminate consumption and
656 ettringite formation are included in Eqs. (26) - (29).
657
658

$$\frac{1}{-a}\frac{\partial Al}{\partial t} = \frac{1}{-b}\frac{\partial SO_4^{2-}}{\partial t} = \frac{1}{c}\frac{\partial C_6 A\bar{S}_3 H_{32}}{\partial t} \tag{25}$$

First-order rate law   Second-order rate law

$$\frac{\partial Al}{\partial t} = -k_1 \frac{a}{b}[SO_4^{2-}] \tag{26}$$ $$\frac{\partial Al}{\partial t} = -k_2 \frac{a}{b}[SO_4^{2-}][Al] \tag{28}$$

$$\frac{\partial C_6 A\bar{S}_3 H_{32}}{\partial t} = \frac{c}{b}k_1[SO_4^{2-}] \tag{27}$$ $$\frac{\partial C_6 A\bar{S}_3 H_{32}}{\partial t} = \frac{c}{b}k_2[SO_4^{2-}][Al] \tag{29}$$

659
660
661 The use of first-order kinetic laws to quantify the formation rate of ettringite and
662 gypsum assumes that neither portlandite (calcium) nor aluminate concentrations are
663 reaction-limiting factors. Such a hypothesis may not remain true over the whole
664 duration of the attack, as complete depletion of some of the reactants could occur in
665 some locations. Bary et al. [44] partially tackled this limitation by introducing
666 restrictions on the maximum amount of ettringite formed based on the initial alumina
667 content.
668
669
670 Shazali et al. [42] adopted a multi-ordered chemical reaction rate equation inspired by
671 the work from Saetta et. al [54]. This approach is based on normalized influence

672 functions to represent the effects of temperature, pore water content, sulfate
673 concentration and portlandite availability. Even though the consideration of temperature
674 and humidity in the rate law seems positive, the approach adopted to quantify its effects
675 is not validated and might be too simplified to justify the additional semi-empirical
676 parameters introduced.
677
678
679 *3.2.2. Chemical equilibrium*
680
681
682 The alternative to the approaches based on purely empirical chemical kinetic laws (K) is
683 the calculation of the current chemical equilibrium state by means of a chemical
684 equilibrium code (E). Equilibrium approaches use thermodynamic data of all solid,
685 aqueous and gas species present in the system to predict the concentrations of the
686 constituents on a chemical equilibrium state. This is achieved by finding the
687 concentrations of the chemical species that simultaneously minimizes the Gibbs free
688 energy of the system and satisfies a system of equilibrium constants. The consideration
689 of all constituents complicates the calculations and increases the number of input
690 parameters but provides a full description of the species present in the system
691 throughout the attack.
692
693
694 As shown in Table 6, the consideration of the full composition of the aqueous solution
695 and solid phases is a common feature of all chemical modules that include equilibrium
696 calculations. Thermodynamic modeling of ESA is usually described in terms of
697 equilibrium between the liquid (pore solution) and the solid hydrated phases of the
698 cement paste. In fact, all ESA models reviewed solely account for heterogeneous
699 reactions based on dissolution/precipitation processes of solid hydration products.
700
701
702 Even though the specific phases considered vary slightly in each model, the majority
703 include the following mineral phases: Portlandite, C-S-H gel, ettringite, monosulfate,
704 hydrogarnet, gypsum and sodium sulfate (mirabilite). The aqueous pore solution is
705 usually simulated by the following ionic species: K^+, Na^+, Ca^{2+}, SO_4^{2-}, OH^- and
706 $Al(OH)_4^-$. The dissolution process of the clinker phases is commonly not considered in
707 such calculations since the pore solutions tend to be highly undersaturated with respect
708 to these phases due to its slow dissolution rate [15].
709
710
711 Two conceptually equivalent methods are generally used to calculate chemical
712 equilibrium in ESA models. The most common method consists on solving the system
713 of mass balance and mass action equations known as Law of mass action (LMA). LMA
714 system of equations models the equilibrium condition of the reactions for a given set of
715 species. Dissolution/precipitation reactions are usually simulated by the equilibrium

716 relationship described in Eq. (30) [55]. If the activity product of the ions in solution
717 involved in the reaction is above the solubility product, precipitation occurs to decrease
718 the ionic activity of the reactants. Otherwise, dissolution occurs. Notice that the
719 concentrations of pure solids and liquids are not considered.
720
721

$$K_m = \prod_{i=1}^{N_i} (C_i \gamma_i)^{v_{mi}} \qquad \text{For } m=1,\dots,M \qquad (30)$$

722
723
724 The term K_m corresponds to the solubility constant of the solid phase m. C_i is the
725 concentration of species i in solution and v_{mi} is the stoichiometric coefficient of the ith
726 ion in the mth hydration product. If M number of species are considered to be in
727 equilibrium with the solution, then M simultaneous equations should be solved to
728 determine the concentration of each species at equilibrium. The term γ_i corresponds to
729 the chemical activity coefficient. The activity coefficient is computed in all ESA models
730 reviewed by means of the modified Davies model [13], which is valid for solutions with
731 high ionic strength. The only exception is presented by Schmidt-Döhl and Rostasy
732 [37,38] and Rigo et al. [41], who simulated the activity coefficients of solved ions by
733 the Pitzer theory and the Gibbs-Duhem equation [56,57]. Additionally, mass and charge
734 balance restraints are imposed to assure that no mass is lost or created during
735 precipitation/dissolution processes and that the sum of positive charges equal the sum of
736 negative charges in the system.
737
738
739 Alternatively, chemical equilibrium can be calculated by directly minimizing the Gibbs
740 free energy of the system (GEM). The GEM approach is based on mass and charge
741 balance of the whole system and the equilibrium composition is calculated
742 automatically from the stochiometrically possible phases [15]. The only information
743 required is the stoichiometric coefficients of the concerned chemical species and their
744 thermodynamic data [37,38]. Despite the advantages reported of GEM over LMA [58],
745 only the ESA models from Schmidt-Döhl and Rostasy [37,38] and Rigo et al. [41] adopt
746 this approach (Table 6). This situation might be explained by the complexity of
747 integrating equilibrium solvers based on GEM into the reactive transport calculators.
748
749
750 The coupling of chemical and transport modules has been traditionally approached in
751 two sequential steps. The first step is solely concerned with the resolution of the
752 transport equations presented in section 3.1. The new ionic concentrations are then
753 corrected in a second step to ensure chemical equilibrium between the ions in the pore
754 solution and the different hydrated compounds of the cement paste. Solid phases are
755 dissolved or precipitated accordingly. This loop is repeated for each time step
756 considered in the simulation. The description of the chemical reactions as algebraic

757 mass action equations (LMA method) fits well in this scheme and allows the treatment
758 of the reactive transport phenomenon as a mixed problem involving the solution of
759 algebraic and partial differential equations.

760
761

762 The treatment of the reactive transport phenomenon as two separate sequential
763 algorithms (transport and chemistry) is possible due to the local equilibrium assumption
764 (LEA) adopted by all ESA models that include chemical equilibrium calculations. LEA
765 assumes that the rate of the reaction is large with respect to the ionic and fluid transport
766 processes. This assumption seems reasonable based on the presence of dissolution or
767 precipitations fronts for the main species involved in the ESA within a region close to
768 the external surface of the specimen. This indicates that chemical reactions are the
769 governing process on the reactive transport phenomenon, at least prior to the generation
770 of significant damage [59]. Samson and Marchand [43] corroborated the validity of this
771 assumption for ionic transport problems in cementitious materials based on the
772 dimensionless Damköhler number.

773
774

775 *3.2.3. Combination of kinetic laws and chemical equilibrium*

776
777

778 Finally, some ESA models adopt a third approach consisting on a combination of
779 chemical equilibrium calculations and kinetic laws [37,38,41,48]. These models are
780 mainly based on the same principles described for pure equilibrium models. However,
781 the chemical equilibrium equations of certain phases are replaced by kinetic laws to
782 account for phase formation in non-equilibrium conditions.

783
784

785 Bary et al [48] replaces the dissolution/precipitation equation of ettringite by the kinetic
786 law described in Eq. (31). The term k corresponds to the kinetic coefficient expressed as
787 *concentration·time^{-1}*. $Q_{C_6 A\overline{S_3}H_{32}}$ and $K_{C_6 A\overline{S_3}H_{32}}$ are the ion activity and equilibrium
788 solubility product of ettringite, respectively. By adopting this approach, ettringite does
789 not necessarily reach equilibrium at the end of each time step of the simulation, which
790 is a required condition to reproduce crystallization pressures associated to ettringite
791 growth in supersaturated solutions.

792
793

$$\frac{\partial C_6 A\overline{S_3}H_{32}}{\partial t} = k \left(\frac{Q_{C_6 A\overline{S_3}H_{32}}}{K_{C_6 A\overline{S_3}H_{32}}} - 1 \right) \qquad (31)$$

794
795

796 **3.3. Modeling of the expansive forces**

797
798

799 Table 7 examines the main approaches adopted by T-C-E and T-C-E-M models to
800 simulate the expansive forces generated at the pore-level during the ESA.

801
802

803 *3.3.1. Volume increase theory*

804
805

806 Table 7 highlights that expansive forces are usually quantified by the volume increase
807 associated to ettringite formation. The consideration of the volume change caused by
808 other hydration products is not widely implemented, as it requires an advanced chemical
809 module able to compute all hydrated phases in the cement paste. As indicated in Table
810 6, this is not a common feature amongst T-C-E and T-C-E-M models.

811
812

813 Models based on the volume increase theory usually consider that not all aluminate
814 reacted generates expansions, as the pore network is able to accommodate a certain
815 amount of expansive products without exerting any pressure to the pore walls. A
816 pressure on the surrounding walls may be only exerted if the crystals become too large
817 and/or too numerous to fit into the available space. Consequently, the general equation
818 described in section 2.3.1 to estimate local linear expansions (Eq. (9)) is usually
819 modified to capture this phenomenon. Eq. (32) [18] quantifies the capacity to
820 accommodate expansive products by the fraction (f) of the concrete initial connected
821 porosity (φ_0) that has to be filled prior expansion starts.

822
823

$$\varepsilon_l = \text{Max.}\left\{\left[(1 + vV_m CA^r - f\varphi_0)^{1/3} - 1\right], 0\right\} \tag{32}$$

824
825
826 Table 7. Main features of the modeling approaches to simulate ESA expansive forces.

	Ref.	Mechanism		Mode		Expansive phases	Pore network	Buffer capacity
		Vol. increase	Cryst. pressure	Eigenstrain	Eigenstress			
T-C	[36]							
	[39]							
	[21]							
	[43]							
	[20]							
T-C-E	[47]	X		X		Ettringite	1 Pore	$f\varphi_0$
T-C-M	[42]							
T-C-E-M	[37,38][1]							
	[18,40]	X		X		Ettringite	1 Pore	$f\varphi_0$
	[41][1]							
	[44]		X		X	Ettringite	1 Pore	
	[45]	X		X		Ettringite	1 Pore	$f\varphi_0$
	[19]	X		X		All solids	1 Pore	$f\varphi_0$
	[46]	X		X		Ettringite	1 Pore	$f\varphi_0$

[48]	X	X	X	X	Ettringite	1 Pore	$f\varphi_0$
[49]	X		X		Ettringite	N Pores	$f_i\varphi_i$
[50]	X		X		Ettringite	1 Pore	$f\varphi_0$
[51]	X		X		Ettringite	1 Pore	
[52]	X		X		Ettringite	1 Pore	$f\varphi_0$

827 ^{1} Characteristics of this model are not included due to the lack of details provided

The considerations of the overall initial porosity and a unique buffer coefficient assume that all complexity of the concrete porosimetry can be reduced to a single pore where all expansive products precipitate. This is equivalent to say that the precipitation and expansion occur simultaneously in all pores regardless of their size, as the amount of expansive products precipitated in each pore is proportional to its volume. Through this approach, the models are not able to account for expansive pressures generated during early stages of the attack as the expansions computed are null until the amount of ettringite precipitated fills the entire buffered volume ($f\varphi_0$). A schematic representation of the simplifications assumed by Eq. (32) is shown in Figure 3.
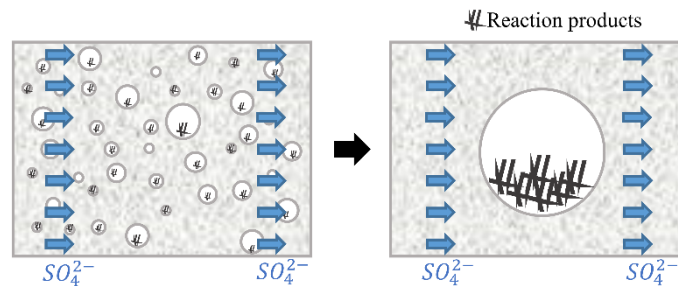
T. Ikumi et al. [49] adopted an alternative methodology to compute expansions to tackle this limitation. The model presented is based on a more realistic representation of the concrete porosimetry by discretizing the real pore size distribution of the material into a finite number of pores, each one representing a volume fraction of the total porosity (φ_i). Then, a parameter referred to as ettringite formation rate is used to quantify and distribute the ettringite formed within the pores considered. The contribution to the total local expansion of each pore size is estimated based on its volume ratio filled by ettringite and its individual capacity to accommodate expansive phases (f_i). This methodology acknowledges that not all ettringite precipitated during the attack contributes with the same weight into the expansive forces generated. Instead, ettringite precipitated in small pores is likely to generate higher and earlier pressures than ettringite growing in larger pores due to a faster filling rate and a smaller capacity to accommodate expansive products.

860 Cefis and Comi [51] present the only model that completely neglects the buffer capacity
861 of the pore network during the estimation of expansive forces. These authors consider
862 that ettringite is formed through a topochemical reaction occurring between the
863 hydrated products of cement and the sulfate. In topochemical reactions the product is
864 formed directly in the surface of the reactants, therefore all volume variation due to
865 ettringite formation is translated into expansive forces. The validity of this approach has
866 been questioned by several authors, who claimed that the crystal structure of C_3A or
867 monosulfate is completely different to that of ettringite, so direct transformation is not a
868 plausible theory [34].
869
870
871 *3.3.1. Crystallization pressure theory*
872
873
874 The number of models quantifying the expansive forces generated through the
875 crystallization pressure theory is minimal (Table 7). The prevalence of the volume
876 increase in modeling might be explained by the combination of two factors. First, the
877 crystallization pressure theory requires the full definition of the activities of ionic
878 species in contact with the ettringite crystals, which is only possible through chemical
879 equilibrium calculations. Second, the algorithm should be able to compute ettringite
880 growth in supersaturated solutions. Notice that the latest requirement is usually not
881 compatible with the first one, as most ESA models able to provide a full description of
882 the ionic species and solid phases are solely based on chemical equilibrium calculations,
883 which guarantees that the solution is never supersaturated with respect to any solid
884 phase in the microstructure.
885
886
887 Bary et al. presents the only model that adopted solely the crystallization pressure
888 theory to simulate the expansive forces generated during the ESA [44]. The authors are
889 able to compute crystallization pressures as the chemical module adopted is based on
890 chemical kinetics, not on equilibrium assumptions. Consequently, Bary et al. do not
891 apply the general equation described in Eqs. (10)-(11), as this model does not provide a
892 full description of the ionic solution and solid phases. Instead, the authors use the
893 simplified version described in Eq. (33), which is only defined by current and
894 equilibrium sulfate and calcium concentrations. It is unclear how calcium and sulfate
895 concentrations at chemical equilibrium ($C^0_{Ca^{2+}}$, $C^0_{SO_4^{2-}}$) are estimated through this kinetic
896 approach.
897
898

$$p = \frac{RT}{V_{Et}} \ln \left(\frac{[C_{Ca^{2+}}]^2 \left[C_{SO_4^{2-}} \right]^2}{[C^0_{Ca^{2+}}]^2 \left[C^0_{SO_4^{2-}} \right]^2} \right) \qquad (33)$$

899
900

901 The model is applied with a relatively good accuracy to predict cracking initiation.
902 However, it leads to macroscopic expansions of about two orders of magnitude lower
903 than typical experimental data [48]. According to the authors, the crystallization
904 pressures developed do not permit generation of sufficient macroscopic strains with the
905 elastic approach adopted. Crystallization pressures of the order of several thousands of
906 MPa would be necessary to get calculated free expansions comparable to measured
907 ones.
908
909
910 Bary et al. presented another ESA model in 2014 that incorporated an alternative
911 approach to explain the macroscopic expansions [48]. This model introduced a
912 macroscopic bulk strain to reproduce the increase of volume caused by secondary
913 ettringite formation through an equivalent equation of Eq. (32). By adding this
914 consideration, the expansions are a result of both the additional volume generated by
915 ettringite formation and the crystallization pressure exerted on the pore walls by the
916 supersaturated solution. In this case, the expansions predicted were similar to the ones
917 obtained in the test. Bary et al. pointed out that the contribution of the crystallization
918 pressure was negligibly small compared to the bulk strain produced by secondary
919 ettringite formation [48]. This may suggest that the model was basically able to
920 reproduce measured expansions due to the application of the volume increase theory.
921
922
923 **3.4. Modeling of the mechanical response**
924
925
926 T-C-M and T-C-E-M models incorporate mechanical modules to convert the
927 degradation processes generated at the pore-scale into actual damage and/or
928 macroscopic expansions. Table 8 shows the characteristics of the main approaches
929 adopted by the selection of models reviewed to simulate the local and non-local
930 mechanical response.
931
932
933 Table 8. Characteristics of the mechanical modules considered in advanced ESA

934 models.

	Ref.	Local mechanical response			Non-local mechanical response	
		Stress-induced cracking		Chemical-induced strength loss	Tenso-deformational analysis (macro expansions)	Stress-induced cracking
		Isotropic damage variable	Discrete interface elements	Isotropic damage variable		Discrete interface elements
T-C	[36]					
	[39]					
	[21]					
	[43]					
	[20]					
T-C-E	[47]					

T-C-M	[42]			X		

T-C-E-M	[37,38][1]					
	[18,40]	X			X	
	[41][1]					
	[44]	X			X	
	[45]	X			X	
	[19]	X				
	[46]		X		X	X
	[48]	X			X	
	[49]	X			X	
	[50]	X				
	[51]	X		X	X	
	[52]	X				

[1] Characteristics of this model are not included due to the lack of details provided

3.4.1. Local mechanical response

The local mechanical response accounts for the damage generated within the region directly affected by sulfate penetration. In this region, models recognize the generation of damage associated to the expansive forces (referred to as stress-induced cracking in Table 8) and the decalcification of hydrated phases (referred to as chemical-induced strength loss in Table 8). T-C-M models can only compute chemical damage while T-C-E-M models are potentially able to account for both, chemical and stress-induced damage.

Stress-induced cracking

Stress-induced microcracking has been traditionally reproduced by a damage variable based on continuum damage mechanics. The early approach presented by Tixier and Mobasher [18] has been widely implemented and served as a basis for most of the models developed (e.g. [19,50,52]). In this case, the constitutive response of the material is simulated by a simple uniaxial stress-strain law that related the local strains with the damage developed. The damage is quantified by an isotropic scalar variable usually ranging from 0 to 1 based on a crack density parameter. Three regions are usually defined [18]:

- Linear-elastic response: The material is considered undamaged,
- Prepeak region: Microcrack initiation leading to a linear decrease of the mechanical properties and/or increase of diffusivity,

967 • Postpeak region: Microcracks coalesce into a single main crack and the
968   deformation is represented as the opening of a single dominant crack with a
969   gradual decrease in the load-carrying capacity of the matrix.
970
971
972 Approaches based on continuum damage mechanics have important limitations when it
973 comes to predict crack patterns or the spalling effects. For example, Sarkar et al. [19]
974 adopt a failure criterion based on an arbitrary number of elements of the discretization
975 reaching the maximum damage state, without any mechanical justification. However,
976 this approach might be sufficient to identify crack appearance and estimate an
977 approximate crack pattern [44].
978
979
980 The model presented by Idiart et al. [46] represents an important contribution in this
981 field. The main feature of this model is the nonlinear fracture mechanics-based crack
982 propagation procedure, which considers the effect of cracking explicitly in the
983 degradation process. For that, zero-thickness interface elements are introduced in all the
984 aggregate–matrix contacts and also in predetermined locations within the matrix. Notice
985 that this model is able to capture accurately the main crack patterns inside and outside
986 the region directly affected by sulfate penetration.
987
988
989 *Chemically-induced strength loss*
990
991
992 Even though all models included in Table 8 incorporate chemical modules to account
993 for the chemical reactions triggered by sulfate penetration, there are only two models
994 that quantify the chemical damage associated [42,51]. Shazali and coworkers [42]
995 assume that the strength loss experienced by concrete is entirely caused by the
996 decalcification of hydrated phases due to gypsum formation. Chemical damage is
997 quantified by a local relative strength loss (pnL) function that represents an empirical
998 relation between the degree of reaction (G_n) and the loss of strength (Eq. (34)). The
999 terms a and m correspond to fitting parameters defined on the basis of experimental
1000 data.
1001
1002

$$pnL = (1 - a^{-m})\left[1 - \frac{1}{1 + (aG_n)^m}\right] \qquad (34)$$

1003
1004
1005 The model presented by Cefis and Comi is the only model that accounts for both
1006 chemical damage and expansive forces [51]. In this case, it is considered that the
1007 decalcification of concrete causes the formation of diffuse microcracks. Similarly to
1008 [42,60], this phenomenon is quantified by an isotropic damage variable (d) expressed as

a function of the reaction extent ($\bar{\xi}$) (Eq. (35)). Where r_1, r_2 and r_3 are material dependent parameters. Unfortunately, from the results presented it is not possible to distinguish the relative weight of chemical damage into the overall degradation obtained.

$$d = \frac{1 - \exp(-r_1\bar{\xi})}{1 + \exp(-r_1\bar{\xi} + r_2)} r_3 \tag{35}$$

3.4.2. Non-local mechanical response

It seems common sense that a large pile of 2 m diameter should be more durable against the ESA than a micro-pile of 30 cm diameter under the same exposure conditions. Unlike internal degradation processes, the region directly affected by sulfate penetration is usually restricted to a few centimeters close to the external surface. The sound region, which in most real structures constitutes a larger area, contributes to reduce the damage caused by the attack due to equilibrium and compatibility with the damaged area. Several recent works highlight the importance of the size of the element on ESA resistance [10,59].

Table 8 shows that the majority of models quantifying damage include a full tenso-deformational analysis on the whole section of the attacked element to account for these phenomena. By that, these models are able to quantify macroscopic expansions over time and estimate the stress distribution generated inside and outside the attacked region. Damage estimations in models without tenso-deformational analyses might not correspond well with reality, especially in structures with large sound/damaged region ratios.

Stress distribution monitoring on the whole section of the element opens up the possibility to account for damage generation outside the regions directly affected by sulfate penetration. However, Table 8 indicates that this is not commonly implemented in ESA models. In fact, the only model able to account for the energy dissipated in the fracture processes outside the penetrated region is the one presented by Idiart et al. [46]. The approach adopted by the authors is explained in section 3.4.1.

3.5. ESA Model selection

1050 The review presented in sections 3.1-3.4 highlights a large pool of models available
1051 based on different approaches and principles with varying degrees of complexity. This
1052 wide variety of options often confuse practitioners in the selection of the appropriate
1053 model to use for each application. Numerical models are commonly used to provide key
1054 data to support decision-making on different aspects related to ESA durability. For each
1055 project, the information desired varies depending on its particular needs. For example,
1056 in some structures the durability requirements might be defined in terms of limitations
1057 on the penetration of external agents, while in other applications the main concerns
1058 might be related to the dimensional stability or crack formation.
1059
1060
1061 As not all models reviewed are able to provide the same information, the selection of a
1062 suitable model involves pairing of the required data with the outputs of the numerical
1063 model. For that, it is essential to understand the capabilities of each model reviewed in
1064 terms of the outcomes provided. Table 9 relates typical required data during ESA
1065 assessments with the qualified models able to provide such information. The required
1066 data listed covers different aspects associated to the transport process, the chemical
1067 reactions and the mechanical response of the attacked element. Notice that Table 9 is
1068 purely defined by the potential capabilities of the models and the actual accuracy of the
1069 predictions is not considered here.
1070
1071
1072 Table 9. Qualified models for the most common desired outputs in ESA assessments.

Desired outputs	Qualified models			
	T-C	T-C-E	T-C-M	T-C-E-M
Transport Sulfate concen.	[36][39][21][43][20]	[47]	[42]	[30][10][41][44][45][19][46][48][49][50][51][52]
Calcium concen.	[21][43][20]			[30] [41][44] [19] [48] [50]
Full ionic concen.	[21][43][20]			[30] [41] [19] [48] [50]
Chemical Ettringite concen.	[21][43][20]			[30] [41][44][45][19] [48] [50]
Gypsum concen.	[21][43][20]		[42]	[30] [41][44] [19] [48] [50]
Aluminate concen.	[21][43][20]	[47]		[30][10][41] [19][46][48][49][50][51][52]
Full phase comp.	[21][43][20]			[30] [41] [19] [48] [50]
Mechanical Chem. strength loss			[42]	[51]
Local cracking				[10] [44][45][19][46][48][49][50][51][52]
Non-local cracking				[46]
Expansions				[10] [44][45] [46][48][49] [51]

1073
1074
1075
1076 As expected, the eligible options diminish with the increase of complexity of the
1077 outcomes desired. All models reviewed are able to provide a basic outcome such as the
1078 sulfate concentration during the attack. However, the number of options is reduced by a
1079 factor of 3 when the required data are the expansions evolution. If the chemical strength
1080 loss caused by decalcification or non-local cracking are to be quantified, the number of
1081 qualified models is dramatically reduced.

4. RESEARCH PRIORITIES

This section aims to identify the major areas that currently compromise the accuracy of the assessments provided by ESA models based on the review presented in section 3. The literature review features ESA models with advanced transport and chemical modules (e.g. [20,21,43,48,50]) able to provide full ionic and phase composition during the attack and account for several transport mechanisms. The high degrees of sophistication may be attributed to the traditional perception of the ESA as a pure chemical attack, which led to focus efforts on the simulation of the reactive-transport process.

Additionally, the modeling of transport and chemical processes shares the same basis as a wide variety of phenomena comprehensively studied during the last decades, such as the transport of contaminants in soils or the thermodynamic modeling of geochemical systems. Contributions made in other areas have been adopted by ESA models, resulting in reactive-transport modules with advanced features. Consequently, the authors do not identify major hurdles related to the simulation of the reactive-transport process that compromise its accuracy.

Reliable estimations of the mechanical response during the ESA require an accurate quantification of the damage mechanisms generated at the micro-scale (chemical damage and expansive forces) and the translation of its effects to the macro-scale. The current state of the art on structural analysis features several advanced methods able to perform this translation precisely, considering the interactions between sound and damage regions of the attacked element (e.g. FEM with fracture-based constitutive laws [46]). Therefore, the validity of the results provided by the mechanical model is greatly defined by the accuracy of the expansive forces and the chemical damage predicted at the pore-level.

Table 9 highlights the shortage of ESA models attempting to quantify the deterioration of the materials mechanical properties caused by leaching and dissolution of calcium bearing phases. The few attempts reported address the simulation of this phenomenon through over simplified approaches with fitting parameters defined on the basis of experimental data not easily acquirable. Additional research is required to provide accurate estimations of the chemical damage and enable a widespread incorporation of this phenomenon in advanced ESA models.

As discussed in the review, the majority of numerical models acknowledge the expansive forces generated at the pore-scale as the main degradation mechanism associated with ESA. The lack of consensus on the mechanism by which the presence (or formation) of ettringite causes overall expansion and cracking have been translated into the modeling field. Even though the volume increase theory does not currently stand as the most plausible theory due to its simplicity, most numerical models have adopted this approach to simulate the expansive forces generated.

Estimations provided through this approach are strongly influenced by the capacity of the pore network of the material to accommodate expansive phases. However, there is not any reliable quantification of this parameter. Consequently, models adopt different values arbitrarily, often treating this variable as a fitting parameter. The early works of Atkinson and Hearne [4], and Clifton and Pommersheim [9] assumed that only 5 % of the volume of ettringite formed was translated into actual expansions. Clifton and Pommersheim [9] additionally considered that expansion occurs only when the reaction products fill the entire volume of capillary porosity ($f=100$ %). More recently, Tixier and Mobasher fixed this parameter in a range between 5 % - 40 % of the initial porosity [18,61]. Basista and Weglewski [45] and Yu et al. [50] arbitrarily assumed it to be 50 and 36 %, respectively. Discrepancies of such ranges question the accuracy of the assessments. The role of porosity during the attack should be further studied in order to provide procedures or guidelines to estimate the capacity of a specific material to accommodate expansive phases.

The simulation of expansive forces through the crystallization pressure theory is still at an early stage and the few attempts reported are still far from being able to reproduce the real behavior of specimens exposed to ESA. The models that adopted this approach are unable to reproduce the main feature of this theory, which is that only ettringite growing in small pores is likely to build up enough pressure to cause damage. To capture this phenomenon it is necessary to consider a more realistic representation of the pore network and be able to account for ettringite growth in different locations within the pore structure based on local saturation conditions. This is not compatible with current ESA reactive-transport models. Further research is needed to assess the viability of this modeling approach and justify the increase of computational complexity involved over the simpler volume increase theory.

5. CONCLUSIONS

This review of the most representative ESA models developed during the last 20 years identified the most common modeling approaches adopted and the capabilities and limitations associated with each one of them. It is important to highlight that in this

paper, the term ESA exclusively refers to the degradation triggered by chemical reactions between sulfate ions and the cement paste. The simulation of damage attributed to physical sulfate attack such as crystallization of water-soluble sulfate salts is not addressed. The following specific conclusions may be derived from the present study:

- A significant number of advanced ESA models do not simulate all of the main processes involved in the ESA (transport process, chemical reactions, generation of expansive forces and the mechanical response), which may limit the scope of the predictions.

- The literature review features models with advanced transport and chemical modules able to provide full ionic and phase composition during the attack and account for several transport mechanisms.

- Practically all models that quantify damage associated with ESA assume that the only source of degradation are the expansive forces generated at the pore network by ettringite formation. Chemical damage associated to the dissolution of calcium-bearing phases is rarely quantified.

- Improvement on the accuracy of the expansive forces estimated at the pore-level and the chemical damage generated in the material are identified as current major research priorities in ESA modeling.

REFERENCES

[1] J. Marchand, I. Odler, J.P. and Skalny, Sulfate attack on concrete, Spon Press, Taylor & Francis Group, New York, 2002.

[2] A. Neville, The confused world of sulfate attack on concrete, Cem. Concr. Res. 34 (2004) 1275–1296. doi:10.1016/j.cemconres.2004.04.004.

[3] S.T. Lee, R.D. Hooton, H.S. Jung, D.H. Park, C.S. Choi, Effect of limestone filler on the deterioration of mortars and pastes exposed to sulfate solutions at ambient temperature, Cem. Concr. Res. 38 (2008) 68–76. doi:10.1016/j.cemconres.2007.08.003.

[4] A. Atkinson, J.A. Hearne, Mechanistic Model for the Durability of Concrete Barriers Exposed to Sulphate-Bearing Groundwaters, MRS Proc. 176 (1989) 149. doi:10.1557/PROC-176-149.

[5] A. Atkinson, D.J. Goult, J.A. Hearne, The influence of wasteform permeability on the release of radionuclides from a repository, Nucl. Chem. Waste Manag. 5 (1985)

203–214. doi:10.1016/0191-815X(85)90079-8.

[6] R. Shuman, V.C. Rogers, R.A. Shaw, The barrier code for predicting long-term concrete performance, Waste Manag. 89 (1989) 701–705.

[7] K.E. Kurtis, P.J.M. Monteiro, S.M. Madanat, Empirical Models to Predict Concrete Expansion Caused by Sulfate Attack, ACI Mater. J. 97 (2000) 156–161. doi:10.14359/818.

[8] P.J.M. Monteiro, K.E. Kurtis, Experimental asymptotic analysis of expansion of concrete exposed to sulfate attack, ACI Mater. J. 105 (2008) 62–71.

[9] J.R. Clifton, J.M. Pommersheim, Sulfate attack of cementitious materials: Volumetric relations and expansions, NISTIR 5390, Natl. Inst. Stand. Technol. (1994) 22.

[10] T. Ikumi, S. Cavalaro, I. Segura, C. Goodier, S. Austin, Simplified analytical assessment of damage induced by the external sulphate attack in concrete piles, in: High Tech Concr. Where Technol. Eng. Meet - Proc. 2017 Fib Symp., 2017. doi:10.1007/978-3-319-59471-2_260.

[11] C. Hall, W.D. Hoff, Water transport in brick, stone and concrete, CRC Press, Taylor & Francis, 2009.

[12] M.A. Rahman, M.Z. Saghir, Thermodiffusion or Soret effect: Historical review, Int. J. Heat Mass Transf. 73 (2014) 693–705. doi:10.1016/J.IJHEATMASSTRANSFER.2014.02.057.

[13] E. Samson, G. Lemaire, J. Marchand, J.J.J. Beaudoin, Modeling chemical activity effects in strong ionic solutions, Comput. Mater. Sci. 15 (1999) 285–294. doi:10.1016/S0927-0256(99)00017-8.

[14] S. Siegesmund, R. Snethlage, Stone in Architecture. Properties, Durability., 2014. doi:10.1007/978-3-642-14475-2.

[15] M. Alexander, A. Bertron, N. De Belie, Performance of Cement-Based Materials in Aggressive Aqueous Environments, Springer, 2013. doi:10.1007/978-94-007-5413-3.

[16] J.A. Dean, Lange's Handbook of chemistry, 1985. doi:10.1016/S0016-0032(40)90947-4.

[17] O.S. Baghabra Al-Amoudi, Attack on plain and blended cements exposed to aggressive sulfate environments, Cem. Concr. Compos. 24 (2002) 305–316. doi:10.1016/S0958-9465(01)00082-8.

[18] R. Tixier, B. Mobasher, Modeling of Damage in Cement-Based Materials Subjected to External Sulfate Attack. I: Formulation, J. Mater. Civ. Eng. 15 (2003) 305–313. doi:10.1061/(ASCE)0899-1561(2003)15:4(305).

[19] S. Sarkar, S. Mahadevan, J.C.L. Meeussen, H. van der Sloot, D.S. Kosson, Numerical simulation of cementitious materials degradation under external sulfate attack, Cem. Concr. Compos. 32 (2010) 241–252. doi:10.1016/j.cemconcomp.2009.12.005.

[20] B. Lothenbach, B. Bary, P. Le Bescop, T. Schmidt, N. Leterrier, Sulfate ingress in Portland cement, Cem. Concr. Res. 40 (2010) 1211–1225. doi:10.1016/j.cemconres.2010.04.004.

[21] Y. Maltais, E. Samson, J. Marchand, Predicting the durability of Portland cement systems in aggressive environments - Laboratory validation, Cem. Concr. Res. 34

1258   (2004) 1579–1589. doi:10.1016/j.cemconres.2004.03.029.

1259   [22] S. Kumar, C.V.S. Kameswara Rao, Effect of sulfates on the setting time of cement

1260   and strength of concrete, Cem. Concr. Res. 24 (1994) 1237–1244. doi:10.1016/0008-

1261   8846(94)90108-2.

1262   [23] B. Mota, T. Matschei, K. Scrivener, The influence of sodium salts and gypsum on

1263   alite hydration, Cem. Concr. Res. 75 (2015) 53–65.

1264   doi:10.1016/j.cemconres.2015.04.015.

1265   [24] W. Kunther, B. Lothenbach, K.L. Scrivener, On the relevance of volume increase

1266   for the length changes of mortar bars in sulfate solutions, Cem. Concr. Res. 46 (2013)

1267   23–29. doi:10.1016/j.cemconres.2013.01.002.

1268   [25] H.F.W. Taylor, Cement chemistry, Cem. Concr. Compos. 20 (1998) 335.

1269   doi:10.1016/S0958-9465(98)00023-7.

1270   [26] W. Hummel, U. Berner, E. Curti, F.J. Pearson, T. Thoenen, Nagra/PSI Chemical

1271   Thermodynamic Data Base 01/01, 2002.

1272   [27] T. Thoenen, D. Kulik, Nagra/PSI chemical thermodynamic database 01/01 for the

1273   GEM-Selektor (V.2-PSI) geochemical modeling code, 2003.

1274   [28] R.J. Flatt, G.W. Scherer, Thermodynamics of crystallization stresses in DEF, Cem.

1275   Concr. Res. 38 (2008) 325–336. doi:10.1016/j.cemconres.2007.10.002.

1276   [29] G.W. Scherer, Stress from crystallization of salt, Cem. Concr. Res. 34 (2004)

1277   1613–1624. doi:10.1016/j.cemconres.2003.12.034.

1278   [30] G.W. Scherer, Crystallization in pores, Cem. Concr. Res. 29 (1999) 1347–1358.

1279   doi:10.1016/S0008-8846(99)00002-2.

1280   [31] K.L. Scrivener, H.F.W. Taylor, Delayed ettringite formation: a microstructural and

1281   microanalytical study, Adv. Cem. Res. 5 (1993) 139–146.

1282   doi:10.1680/adcr.1993.5.20.139.

1283   [32] W. Müllauer, R.E. Beddoe, D. Heinz, Sulfate attack expansion mechanisms, Cem.

1284   Concr. Res. 52 (2013) 208–215. doi:10.1016/j.cemconres.2013.07.005.

1285   [33] K. Tosun, B. Baradan, Effect of ettringite morphology on DEF-related expansion,

1286   Cem. Concr. Compos. 32 (2010) 271–280. doi:10.1016/j.cemconcomp.2010.01.002.

1287   [34] C. Yu, W. Sun, K. Scrivener, Mechanism of expansion of mortars immersed in

1288   sodium sulfate solutions, Cem. Concr. Res. 43 (2013) 105–111.

1289   doi:10.1016/j.cemconres.2012.10.001.

1290   [35] P. Klieger, J.F. Lamond, Significance of tests and properties of concrete and

1291   concrete-making materials, ASTM, 1994. doi:10.1520/STP169C-EB.

1292   [36] P.N. Gospodinov, R.F. Kazandjiev, T. a. Partalin, M.K. Mironova, Diffusion of

1293   sulfate ions into cement stone regarding simultaneous chemical reactions and resulting

1294   effects, Cem. Concr. Res. 29 (1999) 1591–1596. doi:10.1016/S0008-8846(99)00138-6.

1295   [37] F. Schmidt-Döhl, F.S. Rostásy, A model for the calculation of combined chemical

1296   reactions and transport processes and its application to the corrosion of mineral-building

1297   materials Part I. Simulation model, Cem. Concr. Res. 29 (1999) 1039–1045.

1298   doi:10.1016/S0008-8846(99)00087-3.

1299   [38] F. Schmidt-Döhl, F.S. Rostásy, A model for the calculation of combined chemical

1300   reactions and transport processes and its application to the corrosion of mineral-building

1301   materials Part II. Experimental verification, Cem. Concr. Res. 29 (1999) 1047–1053.

1302   doi:10.1016/S0008-8846(99)00094-0.

1303   [39] M.K. Mironova, P.N. Gospodinov, R.F. Kazandjiev, The effect of liquid push out

1304   of the material capillaries under sulfate ion diffusion in cement composites, (n.d.).

1305   [40] R. Tixier, B. Mobasher, Modeling of damage in cement-based materials subjected

1306   to external sulfate attack. II: Comparison with experiments, J. Mater. Civ. Eng. 15

1307   (2003) 314–322. doi:10.1061/(ASCE)0899-1561(2003)15:4(314).

1308   [41] E. Rigo, F. Schmidt-Döhl, M. Krauß, H. Budelmann, Transreac: A model for the

1309   calculation of combined chemical reactions and transport processes and its extension to

1310   a probabilistic model, Cem. Concr. Res. 35 (2005) 1734–1740.

1311   doi:10.1016/j.cemconres.2004.10.004.

1312   [42] M.A. Shazali, M.H. Baluch, A.H. Al-Gadhib, Predicting Residual Strength in

1313   Unsaturated Concrete Exposed to Sulfate Attack, J. Mater. Civ. Eng. 18 (2006) 343–

1314   354. doi:10.1061/(ASCE)0899-1561(2006)18:3(343).

1315   [43] E. Samson, J. Marchand, Modeling the transport of ions in unsaturated cement-

1316   based materials, Comput. Struct. 85 (2007) 1740–1756.

1317   doi:10.1016/j.compstruc.2007.04.008.

1318   [44] B. Bary, Simplified coupled chemo-mechanical modeling of cement pastes

1319   behavior subjected to combined leaching and external sulfate attack, Int. J. Numer.

1320   Anal. Methods Geomech. 32 (2008) 1791–1816. doi:10.1002/nag.696.

1321   [45] M. Basista, W. Weglewski, Chemically Assisted Damage of Concrete: A Model of

1322   Expansion Under External Sulfate Attack, Int. J. Damage Mech. 18 (2009) 155–175.

1323   doi:10.1177/1056789508097540.

1324   [46] A.E. Idiart, C.M. López, I. Carol, Chemo-mechanical analysis of concrete cracking

1325   and degradation due to external sulfate attack: A meso-scale model, Cem. Concr.

1326   Compos. 33 (2011) 411–423. doi:10.1016/j.cemconcomp.2010.12.001.

1327   [47] X.B. Zuo, W. Sun, C. Yu, Numerical investigation on expansive volume strain in

1328   concrete subjected to sulfate attack, Constr. Build. Mater. 36 (2012) 404–410.

1329   doi:10.1016/j.conbuildmat.2012.05.020.

1330   [48] B. Bary, N. Leterrier, E. Deville, P. Le Bescop, Coupled chemo-transport-

1331   mechanical modelling and numerical simulation of external sulfate attack in mortar,

1332   Cem. Concr. Compos. 49 (2014) 70–83. doi:10.1016/j.cemconcomp.2013.12.010.

1333   [49] T. Ikumi, S.H.P. Cavalaro, I. Segura, A. Aguado, Alternative methodology to

1334   consider damage and expansions in external sulfate attack modeling, Cem. Concr. Res.

1335   63 (2014). doi:10.1016/j.cemconres.2014.05.011.

1336   [50] Y. Yu, Y.X. Zhang, A. Khennane, Numerical modelling of degradation of cement-

1337   based materials under leaching and external sulfate attack, Comput. Struct. 158 (2015)

1338   1–14. doi:10.1016/j.compstruc.2015.05.030.

1339   [51] N. Cefis, C. Comi, Chemo-mechanical modelling of the external sulfate attack in

1340   concrete, Cem. Concr. Res. 93 (2017) 57–70. doi:10.1016/j.cemconres.2016.12.003.

1341   [52] J. Zhang, M. Sun, D. Hou, Z. Li, External sulfate attack to reinforced concrete

1342   under drying-wetting cycles and loading condition: Numerical simulation and

1343   experimental validation by ultrasonic array method, Constr. Build. Mater. 139 (2017)

1344   365–373. doi:10.1016/j.conbuildmat.2017.02.064.

1345   [53] A.E. Idiart, Coupled analysis of degradation processes in concrete specimens at the

1346   meso-level, Polytechnic University of Catalonia, 2009.

1347   [54] A. Saetta, R. Scotta, R. Vitaliani, Mechanical behavior of concrete under physical-
1348   chemical attacks, J. Eng. Mech. 124 (1998) 1100–1109.

1349   [55] T. Xu, J. Samper, C. Ayora, M. Manzano, E. Custodio, Modeling of non-
1350   isothermal multi-component reactive transport in field scale porous media flow systems,
1351   (1999).

1352   [56] K.S. Pitzer, Activity Coefficients in Electrolyte Solutions, 2nd ed., CRC Press,
1353   1991.

1354   [57] C.E. Harvie, N. Møller, J.H. Weare, The prediction of mineral solubilities in
1355   natural waters: The Na-K-Mg-Ca-H-Cl-SO4-OH-HCO3-CO3-CO2-H2O system to high
1356   ionic strengths at 25°C, Geochim. Cosmochim. Acta. 48 (1984) 723–751.
1357   doi:10.1016/0016-7037(84)90098-X.

1358   [58] A.M.M. Leal, M.J. Blunt, T.C. LaForce, Efficient chemical equilibrium
1359   calculations for geochemical speciation and reactive transport modelling, Geochim.
1360   Cosmochim. Acta. (2014). doi:10.1016/j.gca.2014.01.038.

1361   [59] T. Ikumi, S.H.P. Cavalaro, I. Segura, A. de la Fuente, A. Aguado, Simplified
1362   methodology to evaluate the external sulfate attack in concrete structures, Mater. Des.
1363   89 (2016). doi:10.1016/j.matdes.2015.10.084.

1364   [60] R. Pignatelli, C. Comi, P.J.M. Monteiro, A coupled mechanical and chemical
1365   damage model for concrete affected by alkali–silica reaction, Cem. Concr. Res. 53
1366   (2013) 196–210. doi:10.1016/J.CEMCONRES.2013.06.011.

1367   [61] R. Tixier, B. Mobasher, Modeling of Damage in Cement-Based Materials
1368   Subjected to External Sulfate Attack. II: Comparison with Experiments, J. Mater. Civ.
1369   Eng. 15 (2003) 314–322. doi:10.1061/(ASCE)0899-1561(2003)15:4(314).